doi.org/10.26434/chemrxiv.12088935.v1

Ultralight Covalent Organic Framework/graphene Aerogels with Hierarchical Porosity

Changxia Li, Jin Yang, Pradip Pachfule, Shuang Li, Meng-Yang Ye, Johannes Schmidt, Arne Thomas

Submitted date: 06/04/2020 • Posted date: 08/04/2020

Citation information: Li, Changxia; Yang, Jin; Pachfule, Pradip; Li, Shuang; Ye, Meng-Yang; Schmidt, Johannes; et al. (2020): Ultralight Covalent Organic Framework/graphene Aerogels with Hierarchical Porosity. ChemRxiv. Preprint. https://doi.org/10.26434/chemrxiv.12088935.v1

The fabrication of macroscopic architectures of covalent organic frameworks (COFs) instead of powders is of great significance to fully exploit their chemical functionality and porosity and to enable sufficient diffusion and mass transfer through the material. However, it is still a challenge to achieve the assembly of such 3D hierarchical porous architectures from COFs. Herein, COF/reduced graphene oxide (rGO) aerogels are presented, which are synthesized by a hydrothermal approach. The COFs grow in situ along the surface of the 2D graphene sheets, which are stacked in a 3D fashion, forming an aerogel after freeze-drying, which can be compressed and expanded several times without breaking. Thus, a facile, green and pyrolysis-free synthetic method for ultralight functional materials has been achieved. The COF/rGO aerogel shows excellent absorption capacity (uptake of > 200 g organic solvent/g aerogel), which can be used for removal of various organic liquids from water. Moreover, as active material of supercapacitor devices, the aerogel delivers a high capacitance of 269 F g^{-1} at 0.5 A g^{-1} and superior cycling stability over 5000 cycles, which is among the best results reported for COF-based supercapacitors so far. This work demonstrates a great advance for green synthesis of ultralight materials for environmental and energy applications.

File list (2)

Ultralight covalent organic framework/graphene aerogels with hierarchical porosity

Changxia Li, Jin Yang, Pradip Pachfule, Shuang Li, Meng-Yang Ye, Johannes Schmidt and Arne Thomas*

Department of Chemistry, Division of Functional Materials, Technische Universität Berlin, Hardenbergstraße 40, 10623 Berlin, Germany.

***e-mail:** arne.thomas@tu-berlin.de

The fabrication of macroscopic architectures of covalent organic frameworks (COFs) instead of powders is of great significance to fully exploit their chemical functionality and porosity and to enable sufficient diffusion and mass transfer through the material. However, it is still a challenge to achieve the assembly of such 3D hierarchical porous architectures from COFs. Herein, COF/reduced graphene oxide (rGO) aerogels are presented, which are synthesized by a hydrothermal approach. The COFs grow in situ along the surface of the 2D graphene sheets, which are stacked in a 3D fashion, forming an aerogel after freeze-drying, which can be compressed and expanded several times without breaking. Thus, a facile, green and pyrolysis-free synthetic method for ultralight functional materials has been achieved. The COF/rGO aerogel shows excellent absorption capacity (uptake of > 200 g organic solvent/g aerogel), which can be used for removal of various organic liquids from water. Moreover, as active material of supercapacitor devices, the aerogel delivers a high capacitance of 269 F g^{-1} at 0.5 A g^{-1} and superior cycling stability over 5000 cycles, which is among the best results reported for COF-based supercapacitors so far. This work demonstrates a great advance for green synthesis of ultralight materials for environmental and energy applications.

Covalent organic frameworks (COFs) are highly porous crystalline polymers constructed from lightweight elements such as C, N, O, B, Si and H by strong covalent bonds among the organic linkers[1-4]. Because of their structural diversity, permanent porosity, long-range order and the versatile functionalities, which can be introduced into the organic backbone, COFs are promising materials for a range of applications such as catalysis[5], gas storage[6], molecular separations[7-8], energy storage[9], etc. However, the traditional synthetic methods for COFs usually demand vacuum conditions, high boiling point organic solvents such as mesitylene or 1,4-dioxane and long reaction times (usually 48–72 h)[10-12]. More importantly, the resulting COFs are usually formed as powders, which are hardly processable as they are insoluble and infusible. The powder form is also detrimental to a possible electric conductivity, observed in conjugated COFs. Finally, their stacked 2D structure with micro- or small mesopores impedes mass or electron transfer and an efficient utilization of the large accessible surface area. Indeed, it is commonly observed that the theoretical surface area of COFs is much higher than the measured ones, which points to dead ends and inaccessible regions within the COF structure, even for small gas molecules. Recently, crystalline and hierarchical porous COFs with macropores and inherent micropores have been synthesized by employing a polystyrene spheres mediated templating method[13]. However, these COFs are also observed as powders, which can be applied e.g. in electrochemical applications just by gluing them to an existing electrode. The direct fabrication of COFs into stable 3D architectures with control over several length scales is thus still a significant challenge and desirable for many practical applications.

Graphene oxide (GO) is considered as an ideal precursor for the assembly of extended architectures due to not only its hydrophilic surface and large surface area, but also their ability to easily create versatile composite structures with a variety of emerging material classes[14-16]. As example, GO was used to prepare graphene/MXene

hydrogels[17-18], graphene-supported metal organic framework (MOF)[19], graphitic carbon nitride (g-C_3N_4) nanoribbon/graphene composites[20], and boron nitride nanotubes/reduced graphene oxide (rGO) aerogels[21]. In these composites not only the beneficial properties of the single compounds is retained, but they also additionally show enhanced electrical conductivity and mechanical property, both endowed by graphene. In this study, COF/rGO composites are prepared by a hydrothermal approach, which yield 3D, hierarchically porous, ultralight and monolithic structures. These novel composite materials are further applied for removal of oil and various organic liquids from water and as an active material of supercapacitor-based energy storage device.

First, a COF/rGO hydrogel was obtained by the in-situ reaction of the organic linkers 1,3,5-Triformylphloroglucinol (Tp) and Diaminoanthraquinone (Dq) in presence of GO. The hydrothermal reaction conditions lead to the reduction of GO to rGO and the uniform growth of TpDq-COF along the surface of rGO nanosheets, yielding an intimate mixing of both phases. After freeze-drying of the obtained hydrogel, a COF/rGO aerogel is finally formed, exhibiting a hierarchical porous structure. Furthermore, the COF/rGO aerogel shows a low density, good conductivity, redox activity and good mechanical strength, yielding excellent absorption and electrochemical properties.

Results

Materials synthesis and characterization. TpDq-COF herein was synthesized by a hydrothermal method, which is scalable, environmentally friendly and time effective. The TpDq COF forms via a Schiff-base condensation between the aldehyde and amine-groups of the respective monomers (Tp and Dq) using p-Toluenesulfonic acid (PTSA) as catalyst (Supplementary Figs. 1 and 2a). Herein, TpDq-COF was chosen because of its redox-activity due to the presence of anthraquinone moieties within its backbone, high chemical stability and large surface area[22-23].

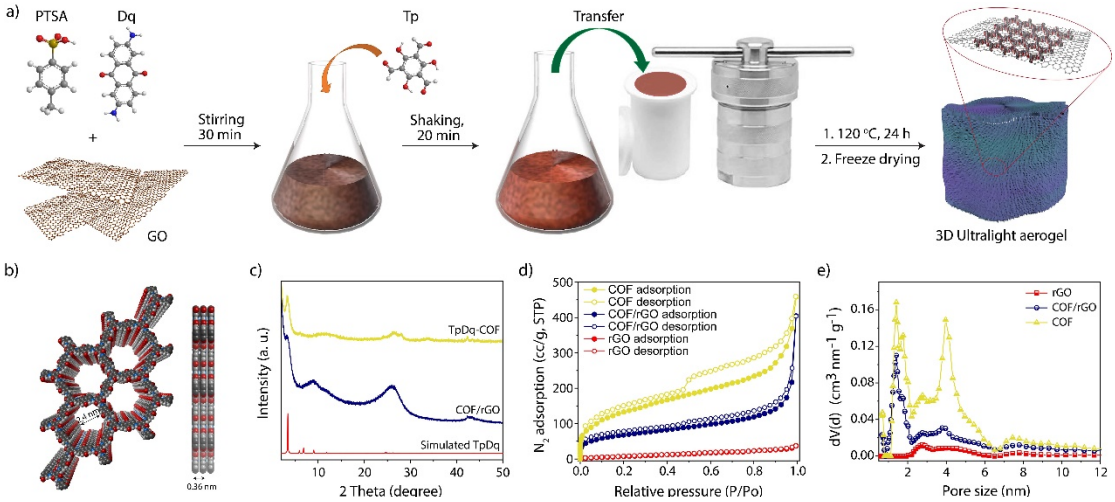

Fig. 1 Schematic representation of 3D ultralight COF/rGO aerogel synthesis. a, Scheme of the synthetic procedure for the preparation the COF/rGO aerogel. **b**, Space-filled model of TpDq-COF from top and side views. **c**, PXRD patterns of the pure COF, COF/rGO and their comparison with simulated XRD pattern from modelled structure in eclipsed form. **d**, N_2 adsorption-desorption isotherms of rGO, COF/rGO and COF. **e**, Pore size distribution for rGO, COF/rGO and COF obtained using the NLDFT method.

When GO is added to the reaction solution, a COF/rGO aerogel is formed during the hydrothermal treatment via self-assembly and subsequent freeze-drying, as illustrated in Fig. 1a and Supplementary Fig. 2b. Briefly, Dq and PTSA were first mixed in water to form an organic salt[24], which was then added to GO solution and stirred at room temperature to form a homogeneous dispersion. Tp was added to the dispersion and shaken thoroughly using a vortex shaker to form an extremely dense and viscous mixture. This mixture was then transferred into an autoclave and heated at 120 °C in an oven for 24 h to obtain a black hydrogel. The hydrogel was thoroughly washed with distilled water, acetone and water to remove the PTSA and unreacted reagents. After freeze-drying, an ultralight COF/rGO aerogel was obtained. This approach can be easily scaled up when a larger autoclave is used. (Supplementary Fig. 4).

The feasibility of the hydrothermal method for the synthesis of TpDq-COF and

COF/rGO hybrid is demonstrated by powder X-ray diffraction (PXRD), Fourier transform infrared spectroscopy (IR) spectra and X-ray photoelectron spectroscopy (XPS). The complete disappearance of representative peak of GO (2θ = ca. 12°) and the appearance of a new broad peak of graphene at 24° demonstrate that GO was reduced effectively under the hydrothermal condition (Supplementary Fig. 5a). IR and XPS spectra further suggest that the oxygen functional groups of GO have been removed largely during the process (Supplementary Figs. 5b and 6). Both COF and COF/rGO display a peak at 3.4° (2θ) corresponding to the reflection from the (100) plane of TpDq-COF, in good agreement with the corresponding simulated XRD pattern from modeled structure, confirming the formation of the crystalline structure of TpDq-COF (Fig. 1c). The presence of graphene weakens the intensity of COF peaks to some extent. For the pure COF, the broad peak at 26° (2θ) can be assigned to the π-π stacking between the COF layers, which corresponds to the (002) plane. This peak is more pronounced for the COF/rGO. It should be however noted, that this peak is shifted to slightly higher angles than observed for pure rGO (Supplementary Fig. 5a), giving a first hint that the graphene layers are covered by the COF. The IR spectra show the similar peaks for TpDq-COF and COF/rGO hybrid (Supplementary Fig. 7). The strong characteristic peaks at 1240 cm^{-1} (C−N), 1560 cm^{-1} (C=C) and 1615 cm^{-1} (C=O) can be attributed to the formation of the *β*-ketoenamine linked framework structures[23]. The vibration frequency corresponding to the ketone (C=O) of the anthraquinone moiety could be assigned at 1670 cm^{-1}. In contrast to rGO, the XPS survey spectra of COF and COF/rGO clearly displays three visible peaks of C 1s, N 1s and O 1s (Supplementary Fig. 8a). The high-resolution XPS spectra of COF/rGO with the same types of carbon species and nitrogen specie as pure COF, further ensure the formation of the COF in presence of graphene (Supplementary Fig. 8b−d). The amount of COF phase within the composite can be derived from the amount of nitrogen detected by elemental analysis (Supplementary Table 1). If not otherwise stated, the material COF/rGO discussed in the paper refers to the mass ratio of monomers: GO of 1:1 whose COF loading is 58.5%.

N_2 sorption measurements were conducted to examine the surface areas and porosity of COF, COF/rGO and rGO (Fig. 1d,e). N_2 adsorption of the pure COF shows characteristics of a type-I isotherm, with a steep increase at low relative pressure, corroborating the microporosity of TpDq-COF. In addition, the obvious hysteresis of the desorption curves indicates the presence of mesopores. The coexistence of micro- and meso-pores were further ensured by the pore size distributions (PSD) following nonlocal density functional theory (NLDFT). TpDq-COF has a Brunauer−Emmett−Teller (BET) surface area of 498 m^2 g^{-1}. This value is lower than that achieved by conventional solvothermal approach (1124 m^2 g^{-1} ± 422)[10,22], but comparable to that of prepared in water with acetic acid as catalyst (489 m^2 g^{-1})[25]. It should be noted that the lower surface area values for TpDq-COF compared with the theoretical surface area of TpDq-COF (2144 m^2 g^{-1}) could arise from the poor solubility of the aldehyde in water. On the other hand, the specific surface area of rGO is only 37 m^2 g^{-1} due to the strong π-π stacking among graphene sheets. The curve for COF/rGO shows a similar isotherm as for pure COF but with a high nitrogen uptake at high relative pressures, indicating the formation of an additional macroporosity (Fig. 1d). The specific surface area of COF/rGO (246 m^2 g^{-1}) is in between the values observed for the pure COF and rGO respectively, showing that both materials are mixed in the expected approximate 1:1 mass ratio.

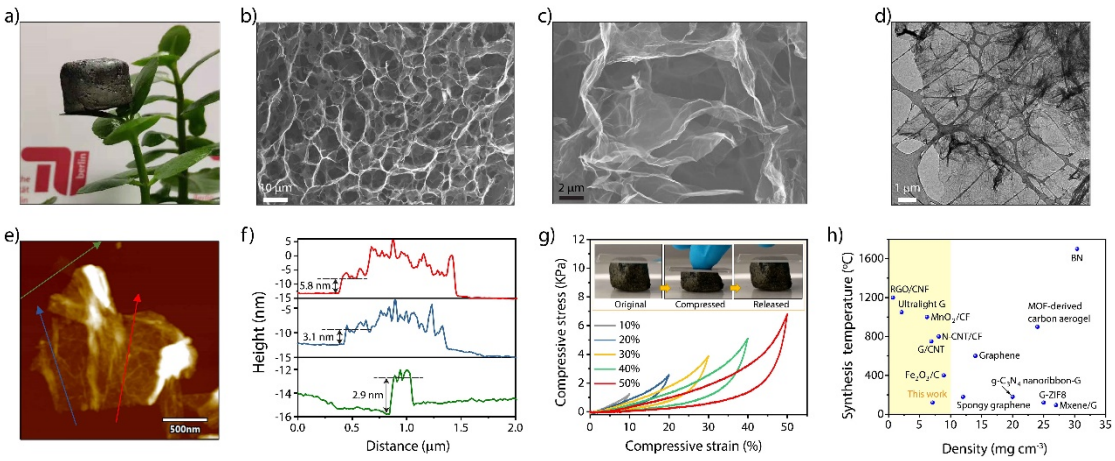

Fig. 2 Structural characterization of 3D COF/rGO. a, A photograph of an ultralight COF/rGO aerogel standing on a leaf. **b**, **c**, SEM images, and **d**, TEM image

of COF/rGO. **e**, **f**, AFM image and the corresponding height profiles for COF/rGO. **g**, The stress-strain curves of COF/rGO aerogel at different maximum strains. The inset images show the snapshots of COF/rGO aerogel under compression and recovering process. **h**, Comparison of density and synthesis temperature of common light-weight materials.

The COF/rGO aerogel have a low density of ca. 7.0 mg cm^{-3} thus can be easily hold by a leaf (Fig. 2a). To gain more insight into the origin of the low density, the morphology and structure of COF, rGO and COF/rGO aerogel were further examined by scanning (SEM) and transmission electron microscopy (TEM). The TpDq-COF possesses a hollow tubular structure (Supplementary Fig. 9). As shown in Fig. 2b and Supplementary Fig. 10, this morphology has completely changed for the COF/rGO composites, as extended and interlinked nanosheets are observed forming a 3D sponge-like structure. The pore sizes of these networks are in the range of several micrometers, which is much smaller than observed for a pure rGO aerogel showing pores of hundreds of micrometers. Notably, no isolated COFs particles were detected on the graphene nanosheets, indicating that the COF grow uniformly along the surface of graphene. TEM images of the COF/rGO sheets confirm that they are very thin and partially wrinkled, pointing to a good flexibility (Fig. 2d and Supplementary Fig. 11). Elemental mapping on these sheets (Supplementary Fig. 11c) show a uniform distributions of C, N and O, further demonstrating that the graphene nanosheets were fully and evenly covered by TpDq-COFs. The morphology of the COF/rGO and graphene was further investigated by atomic force microscopy (AFM) (Fig. 2e–f and Supplementary Figs. 12–13) to elucidate the COF growth on the graphene nanosheets. The COF/rGO nanosheet a minimum thickness of 2.9–6.0 nm; while for rGO sheets with a thickness of 1.5–2.0 nm are found. This increase of average thickness might originate from the uniform loading of a few layers of the COF on the surface of rGO.

The mechanical properties of the COF/rGO aerogel were evaluated by measuring stress−strain curves. As shown in the inset of Fig. 2g and Supplementary Video 1, the

as-prepared aerogel can completely spring back to its original shape after the stress is released. This performance originates from the complete recovery of their 3D porous network after deformation. The compressive stress−strain curves of COF/rGO aerogel with strains up to 10%, 20%, 30%, 40% and 50% are shown in Fig. 2g. During the unloading process, the stress always remaining above zero proving no deformation of the aerogel. The outstanding elasticity originates from the 3D framework structure formed during the hydrothermal process. It should be noted, that the production of most of ultralight carbon-based materials usually requires high temperature annealing[26-31]. In contrary to most of the literature reports, the synthesis temperature of the ultralight COF/rGO aerogel presented herein is very low (120 °C). In addition, the density of 7.0 ± 0.5 mg cm^{-3} is lower than that of pure graphene aerogel and graphene-based composites such as G-ZIF8, g-C_3N_4-G, MXene/G and BN nanotubes/rGO (Fig. 2h) [18-21,29,32-35].

To test the versatility of the formation of composite hydrogels, the GO was mixed with different amounts of the monomers and the resulting mixtures were treated following same protocol (Supplementary Figs. 14−18). With an increase of the amount of monomers, more expanded hydrogels can be obtained. In other words, the COF acts as an expansion agent by inhibiting the stacking of graphene nanosheets, thereby reducing its volume shrinkage. When the amount of monomers was raised to 2:1 related to GO, a highly expanded hydrogel is formed, which however partially loses its shape after freeze-drying probably because of the further weakened interaction between the nanosheets. On the other hand, a COF aerogel cannot be formed without the assistance of GO during the synthesis. Therefore, GO plays a pivotal role in constructing the 3D COF/rGO macrostructures. The aerogels with COF/rGO 0.5:1 and 2:1 show similar IR peaks to COF/rGO 1:1, proving again the formation of the COF structure on graphene (Supplementary Fig. 14c). Moreover, in the PXRD patterns, the peak belonging to (100) plane appearing at 3.4° (2θ) becomes more pronounced (Supplementary Fig. 14d) and the nanosheets becomes thicker (Supplementary Figs. 17,18) with the amount of increasing COF. Therefore, the

aerogel with COF/rGO 1:1 possesses a high COF loading while maintaining intact 3D structure after freeze-drying. More importantly, it also has a relatively low density (Supplementary Table 1).

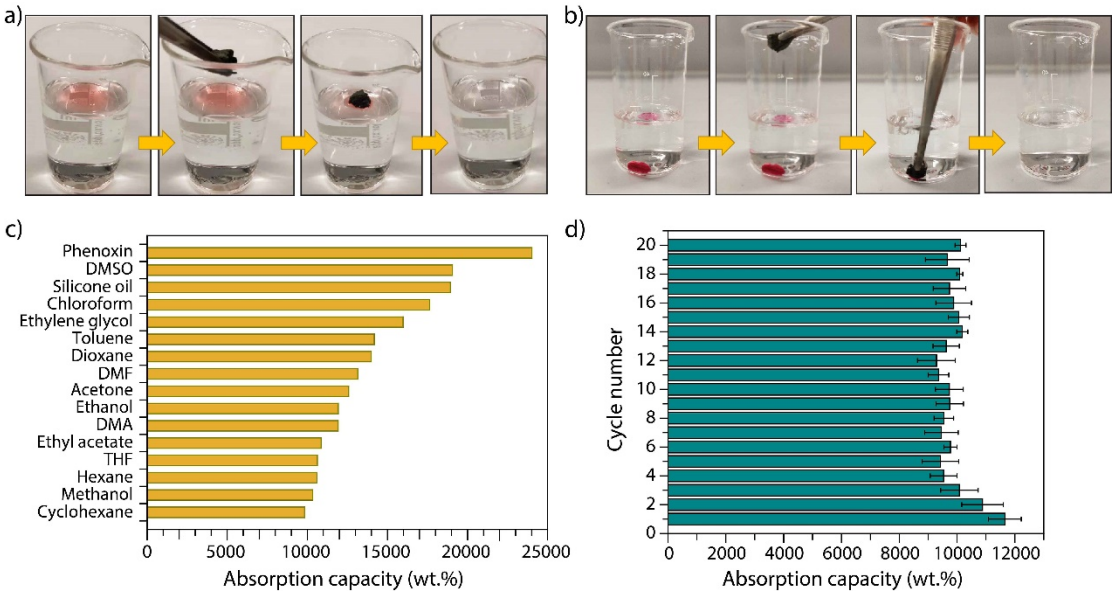

Fig. 3 Absorption performance for oil and other organic solvents of COF/rGO aerogel. Absorption of dyed silicone oil **a**, and chloroform **b**, from water by COF/rGO aerogels. **c**, Adsorption efficiency, and **d**, cycling stability of COF/rGO in terms of weight gain.

Absorption performance. Due to its highly porous structure, high surface area, low density and good mechanical stability, the COF-based aerogel should be a promising absorbent to remove oils and other organic pollutants. To analyze the absorption selectivity, the COF/rGO aerogel was placed on the surface of water and silicon oil mixture, wherein we observed that selective absorption of the floating silicone oil (dyed with Oil Red) within a few seconds (Fig. 3a). Similarly, when aerogel was forced to contact with underwater chloroform (dyed with Oil Red), the quick absorption of chloroform was observed within one second (Fig. 3b; Supplementary Movie 2). After this process, the oil or organic liquid could be separated entirely, thus leaving clean water. The absorption capacity of COF/rGO aerogels was used to

evaluate how much of adsorbed substances was captured. The pure rGO aerogel without COF shows an absorption capacity of 66–93 times its own weight depending on the organic solvents (Supplementary Fig. 19a). The absorption capacities of the hybrid aerogels are much higher, showing the influence of the overall lower density, higher surface area and porosity. The COF/rGO aerogel prepared from monomers: GO ratio of 1:1 has the highest absorption capacity for a variety of organic solvents. Indeed, the COF/rGO aerogels possess an excellent adsorption capacity ranging from 98 to 240 times its own weight, which is higher than that of many reported sorbents (Fig. 3c, Supplementary Table 2 and Supplementary Fig. 19b) [18,30-37]. Moreover, the recyclability of COF/rGO aerogel was measured by repeated ethanol absorption and then drying in the oven. The absorption capacity was found to be maintained above 87% after 20 cycles (Fig. 3d). These results demonstrate the great potential of COF/rGO aerogel as a new candidate for high-efficiency recyclable oil clean-up.

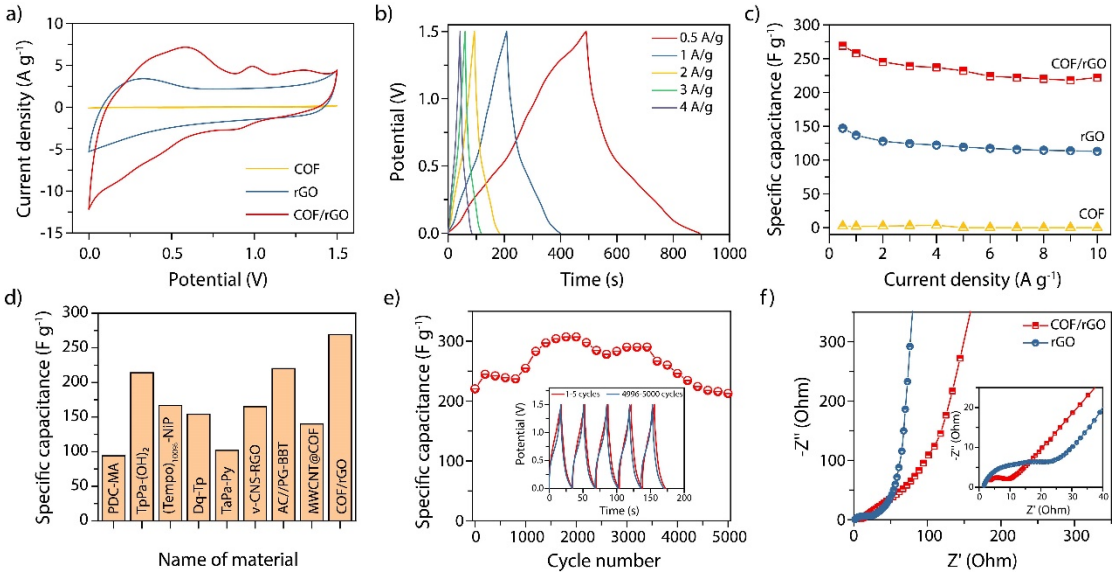

Fig. 4 Performance of COF/rGO electrodes in a symmetrical supercapacitor device. a, CV curves for rGO, COF/rGO and COF at 50 mV s^{-1}. **b**, The galvanostatic charge-discharge curves of COF/rGO at a current density of 0.5, 1, 2, 3 and 4 A g^{-1}. **c**, The specific capacitances calculated from the discharge curves under different current density. **d**, Comparative bar chart expressing the high performance of COF/rGO among all COF-based supercapacitors in two-electrode system. **e**, The cyclic stability

of COF/rGO at a current density of 8 A g^{-1}. **f**, Impedance spectra of the rGO and COF/rGO capacitor.

Electrochemical performance. The development of efficient energy storage equipment is an effective way to solve the long-standing global energy crisis. Apart from the good conductivity and mechanical strength of graphene, Dq in the COFs backbone can act as an active redox unit to provide the pseudocapacitance in electrochemical energy storage. The self-supporting COF/rGO aerogels can be directly used as electrodes of supercapacitor without conducting additives or binders (Supplementary Fig. 20). Electrochemical measurements were carried out by both cyclic voltammetry (CV) and galvanostatic charge/discharge (GCD) experiments for all samples using two electrode cells in 0.5 M H_2SO_4 aqueous electrolyte. Fig. 4a compares the CV curves of 3D rGO/COF, rGO and COF at the sweep rate of 50 mV s^{-1} with a wide potential range of 1.5 V. The electrochemical capacitance of pure COF is very poor without any charge and discharge capacity due to its insulation property (Supplementary Fig. 22). As expected, the 3D COF/rGO electrode showed obvious redox peaks with a dramatic increase in capacitance over the pure COF and pure rGO electrodes (detailed description in Supplementary Figs. 21−23). Fig. 4b and Supplementary Fig. 23 show the GCD curves for the 3D COF/rGO, COF, rGO, 0.5:1 and 2:1 based supercapacitors at different current density of 0.5–10 A g^{-1}. The COF/rGO hybrids display triangular shape with partial deformation, whose additional capacitance result from the pseudocapacitance effects induced by redox active anthraquinone. In order to get direct comparison of the capacitive performance, the specific capacitance is calculated at different current densities from the slope of the discharging curve after the IR voltage drop (Fig. 4c and Supplementary Fig. 24). Among them, the COF/rGO aerogel yields the highest specific capacitance of 269 F g^{-1} at the current density of 0.5 A g^{-1}. With the current density increasing to 10 A g^{-1}, the COF/rGO can still deliver a specific capacitance of 222 F g^{-1} with the retention of 83% capacitance (Fig. 4c). Specifically, the maximum specific capacitance of

COF/rGO is the highest value reported for COF-based materials in a two-electrode system (Fig. 4d)[38-45]. The cycling performance test of COF/rGO device reveal a superior retention of 96% after 5000 cycles, suggesting excellent cyclic stability (Fig. 4e). The electrochemical impedance spectroscopy (EIS) was conducted to display the charge and ion transport dynamics (Fig. 4f). In the Nyquist plots, the straight line at the low-frequencies reveals convenient ion transport path, while the small semicircle at the high-frequencies indicates very low internal electrode-electrolyte resistance and efficient charge mobility in the capacitor device[9]. Therefore, it can be concluded that the 3D structure of COF/rGO material is beneficial for the rapid charge transfer and ion diffusion to redox-active sites, providing guarantee for the outstanding electrochemical performance of the supercapacitor.

Discussion

In summary, COF/rGO aerogels have been fabricated by self-assembly at low temperature following green synthesis pathway. As a combined result of their hierarchically porous structure, ultralow density, good mechanical strength and enhanced conductivity, the newly developed 3D aerogels display an improved absorption ability for organic solvents and outstanding capacitive performance, while both are among the highest values so far reported for related materials. Considering the facile preparation and excellent performance, the 3D COF/rGO aerogel could be a new platform material for environmental and energy applications.

Methods

Synthesis of Tp. Tp was synthesized following the previous literature approach[13].

Synthesis of rGO aerogel. GO was prepared from graphite powder using a modified Hummers' method as reported[14]. The 3D rGO aerogel was prepared by hydrothermal reduction of GO aqueous dispersion. Briefly, 4.3 mL of 5 mg mL^{-1} GO solution and 5 mL water were stirred for 2 h. Then, the GO aqueous dispersion (2.3 mg mL^{-1}) was sealed in a 20 mL Teflon-lined autoclave. After heating at 120 ^{o}C in an oven for 24 h, the autoclave was cooled down to room temperature and 3D graphene monolith was

obtained by freeze-drying.

Synthesis of TpDq-COF. Well-ground PTSA (59.4 mg, 0.31 mmol), Dq powder (13.4 mg, 0.056 mmol) and 5 mL of water were mixed thoroughly and shaken well in a vortex shaker for 5 min. Then, 7.8 mg of Tp (0.037 mmol) was added into the yellow solution and shaken for another 20 min. The orange-red solution was transferred into an autoclave and heated at 120 °C for 24 h. Then, the obtained solid was sequentially washed with water, acetone and water to remove unreacted reagents and monomer fragments. Finally, the material was filtered, collected and freeze-dried or oven-dried at 80 ^{o}C.

Synthesis of COF/rGO aerogel. Well-ground PTSA (59.4 mg, 0.31 mmol), Dq (13.4 mg, 0.056 mmol) and 5 mL of water were mixed thoroughly and shaken well in a vortex shaker for 5 min. The yellow solution was added into 4.3 mL of 5 mg mL^{-1} GO dispersion dropwise and stirred for 30 min to obtain the homogeneous mixed solution. Then, 7.8 mg of Tp (0.037 mmol) was added and shaken for 20 min. The viscous solution was transferred into an autoclave and heated at 120 °C for 24 h. Then, the obtained hydrogel was sequentially washed with water, acetone and water. After freeze-drying, the COF/rGO aerogel was obtained. For comparison, another two COF/rGO aerogels with different ratios of monomers and GO were also fabricated under the same conditions, while only changing the mass of PTSA, Dq and Tp to 29.7 mg, 6.7 mg, 3.9 mg or 118.8 mg 26.8 mg, 15.6 mg, respectively. The mass ratios of monomers: GO were 0.5:1 and 2:1, respectively. The obtained COF/rGO aerogels are denoted as 0.5:1 and 2:1, respectively.

Electrochemical Measurement. All the samples as the electrode materials were measured in a symmetric two-electrode supercapacitor device with 0.5 M H_2SO_4 aqueous solution as electrolyte. Each electrode with a thickness of about 2.0 mm was prepared by cutting down the samples by a blade. The Vernier caliper was used to measure its length (L), width (W) and height (H) accurately. A filter paper and two Au plates were used as separator and electron collectors, respectively. The mass of each electrode was calculated according to $m = \rho LWH$, where ρ is the bulk density of

aerogel. Two identical electrodes were used as cathode and anode for the device configuration (Supplementary Fig. 17).

CV curves and electrochemical impedance spectroscopy of the COF/rGO electrodes were investigated on using a Gamry Reference 600 Potentiostat. GCD behaviors were measured on CT3001A LAND battery testing system. The potential range for CV and GCD tests was 0–1.5 V. Before the measurements, the capacitor cell was soaked in the electrolyte for 3 h. The specific gravimetric capacitance (*Cg*) was calculated from galvanostatic discharge curves using the equation: $Cg = 4I\Delta t/m\Delta V$, where I = constant discharge current, Δt = discharge time, m is the total mass of both electrodes, ΔV = discharge voltage excluding the voltage drop (that is, $\Delta V = 1.5\ \text{V} - V_{drop}$).

Absorption measurement. Before the measurements, the samples were degassed in a vacuum oven at 70 °C for 6 h. The samples were immersed in the various organic solvent for 5 min at the room temperature. The weight was recorded before (W_{initial}) and after ($W_{\text{adsorption}}$) absorption to calculate the weight gain. The absorption capacity of the samples was calculated according to $(W_{\text{adsorption}} - W_{\text{initial}}) / W_{\text{initial}} \times 100\%$. The recyclability test was performed for ethanol by repeating the absorption process after heating treatment at 100 °C for 2 h.

Characterization. Powder X-ray diffraction (PXRD) patterns were carried out on a Bruker D8 Advance instrument with Cu Kα radiation (λ=1.54 Å) operating at 40 kV and 40 mA. PXRD patterns were collected at a scanning speed of 2° min^{-1} in the range of 2°–60°. N_2 sorption measurements was measured on a Quantachrome Quadrasorb SI instrument with degassing temperature of 120 °C for 12 h before the measurement. The specific surface areas were calculated by using Brunauer-Emmett-Teller (BET) calculations and the pore size distributions were obtained from the adsorption branch of isotherms by the non-localized density functional theory (NLDFT) model. XPS spectra were conducted on Thermo Fisher Scientific ESCALAB 250Xi. The scanning electron microscope (SEM) measurement were conducted on Gemini SEM 500 low vacuum high-resolution SEM. Thermo-gravimetric analyses (TGA) were carried out on a Mettler Toledo TGA/DSC1 Star System analyzer at a heating rate of 10 °C min^{-1}

under N_2 atmosphere. The Fourier transform infrared spectroscopy (IR) analyses of the samples were performed on Varian 640IR spectrometer equipped with an ATR cell. Transmission electron microscope (TEM) images were performed on FEI Tecnai G^2 20 S-TWIN electron microscope with an operating voltage of 200 kV. STEM measurement was performed with an additional upgrade using a DISS5 scan generator, attached with a BF/ADF/HAADF-STEM detector. Elemental analyses were performed on a Perkin-Elmer 240 elemental analyzer. Atomic Force Microscopy (AFM) was measured on Cypher AFM Microscope Asylum Research c/o Oxford Instruments with AC Mode/Tapping Mode. The AFM data were analyzed by Gwyddion software. The samples for AFM analyses were prepared by dispersing the samples in a mixed solution of ethanol and water, followed by spin coating onto a Si wafer (100). Mechanical property of the aerogels were carried out on Shimadzu AGS-X.

Data availability

The data that support the findings of this study are available from the corresponding authors upon request.

References

(1) Côté, A. P. et al. Porous, Crystalline, Covalent Organic Frameworks. *Science* **310**, 1166−1170 (2005).

(2) Jin, Y. H. et al. Tessellated multiporous two dimensional covalent organic frameworks. *Nat. Rev. Chem.* **1**, 56 (2017).

(3) Huang, N. et al. Covalent organic frameworks: a materials platform for structural and functional designs. *Nat. Rev. Mater.* **1**, 16068 (2016).

(4) Roeser, J. et al. Anionic Silicate Organic Frameworks Constructed from Hexacoordinate Silicon Centres. *Nat. Chem.* **9**, 977−982 (2017).

(5) Xu, H. et al. Stable, crystalline, porous, covalent organic frameworks as a platform for chiral organocatalysts. *Nat. Chem.* **7**, 905–912 (2015).

(6) Zeng, Y. F. et al. Covalent Organic Frameworks for CO_2 Capture. *Adv. Mater.* **28**,

2855–2873 (2016).

(7) Matsumoto, M. et al. Lewis-Acid-Catalyzed Interfacial Polymerization of Covalent Organic Framework Films. *Chem.* **4**, 308–317 (2018).

(8) Dey, K. et al. Nanoparticle Size-Fractionation through Self-Standing Porous Covalent Organic Framework Films. *Angew. Chem. Int. Ed.* **59**, 1161–1165 (2020).

(9) Yusran, Y. et al. Exfoliated Mesoporous 2D Covalent Organic Frameworks for High-Rate Electrochemical Double-Layer Capacitors. *Adv. Mater.* 1907289 (2020).

(10) Pachfule, P. et al. Diacetylene Functionalized Covalent Organic Framework (COF) for Photocatalytic Hydrogen Generation. *J. Am. Chem. Soc.* **140**, 1423−1427 (2018).

(11) Vitaku, E. et al. Phenazine-Based Covalent Organic Framework Cathode Materials with High Energy and Power Densities. *J. Am. Chem. Soc.* **142**, 16−20 (2020).

(12) Acharjya, A. et al. Vinylene-Linked Covalent Organic Frameworks by Base-Catalyzed Aldol Condensation. *Angew. Chem. Int. Ed.* **58**, 14865−14870 (2019).

(13) Zhao, X. et al. Macro/Microporous Covalent Organic Frameworks for Efficient Electrocatalysis. *J. Am. Chem. Soc.* **141**, 6623−6630 (2019).

(14) Xu, Y. et al. Self-Assembled Graphene Hydrogel via a One-Step Hydrothermal Process. *ACS Nano* **4**, 4324−4330 (2010).

(15) Jiang, Y. et al. Versatile Graphene Oxide Putty-Like Material. *Adv. Mater.* **28**, 10287–10292 (2016).

(16) Zhang, P.et al. Vertically Aligned Graphene Sheets Membrane for Highly Efficient Solar Thermal Generation of Clean Water. *ACS Nano* **11**, 5087−5093 (2017).

(17) Chen, Y. et al. $Ti_3C_2T_x$-Based Three-Dimensional Hydrogel by a Graphene Oxide-Assisted Self-Convergence Process for Enhanced Photoredox Catalysis. *ACS Nano* **13**, 295–304 (2018).

(18) Shang, T. et al. 3D Macroscopic Architectures from Self-Assembled MXene Hydrogels. *Adv. Funct. Mater.* **2019**, *29*, 1903960.

(19) Li, C. et al. Decoration of graphene network with metal–organic frameworks for enhanced electrochemical capacitive behavior. *Carbon* **78**, 231−242 (2014).

(20) Zhao, Y. et al. Graphitic Carbon Nitride Nanoribbons: Graphene-Assisted Formation and Synergic Function for Highly Efficient Hydrogen Evolution. *Angew. Chem. Int. Ed.* **53**, 13934–13939 (2014).

(21) Wang, M. et al. Highly Compressive Boron Nitride Nanotube Aerogels. Reinforced with Reduced Graphene Oxide. *ACS Nano* **13**, 7402–7409 (2019).

(22) DeBlase, C. R. et al. β-Ketoenamine-Linked Covalent Organic Frameworks Capable of Pseudocapacitive Energy Storage. *J. Am. Chem. Soc.* **135**, 16821−16824 (2013).

(23) DeBlase, C. R. et al. Rapid and Efficient Redox Processes within 2D Covalent Organic Framework Thin Films. *ACS Nano* **9**, 3178−3183 (2015).

(24) Kandambeth, S. et al. Selective Molecular Sieving in Self-Standing Porous Covalent-Organic-Framework Membranes. *Adv. Mater.* **29**, 1603945 (2017).

(25) Thote, J. et al. Constructing covalent organic frameworks in water via dynamic covalent bonding. *IUCrJ* **3**, 402−407 (2016).

(26) He, S. et al. High performance supercapacitors based on three-dimensional ultralight flexible manganese oxide nanosheets/carbon foam composites. *J. Power Sources* **262**, 391–400 (2014).

(27) Li, C. et al. Ultralight Multifunctional Carbon-Based Aerogels by Combining Graphene Oxide and Bacterial Cellulose. *Small* **13**, 1700453 (2017).

(28) Zhao, Y. et al. A Versatile, Ultralight, Nitrogen-Doped Graphene Framework. *Angew. Chem. Int. Ed.* **51**, 11371–11375 (2012).

(29) Zhang, Y. et al. Broadband and Tunable High-Performance Microwave Absorption of an Ultralight and Highly Compressible Graphene Foam. *Adv. Mater.* **27**, 2049–2053 (2015).

(30) Dong, X. et al. Superhydrophobic and Superoleophilic Hybrid Foam of Graphene and Carbon Nanotube for Selective Removal of Oils or Organic Solvents from the Surface of Water. *Chem. Commun.* **48**, 10660−10662 (2012).

(31) Chen, N. et al. Versatile Fabrication of Ultralight Magnetic Foams and Application for Oil-Water Separation. *ACS Nano* **7**, 6875−6883 (2013).

(32) Xue, Y. et al. Multifunctional Superelastic Foam-Like Boron Nitride Nanotubular

Cellular-Network Architectures. *ACS Nano* **11**, 558−568 (2017).

(33) Bi, H. C. et al. Spongy Graphene as a Highly Efficient and Recyclable Sorbent for Oils and Organic Solvents. *Adv. Funct. Mater.* **22**, 4421−4425 (2012).

(34) Wang, C. et al. Large-Scale Synthesis of MOF-Derived Superporous Carbon Aerogels with Extraordinary Adsorption Capacity for Organic Solvents. *Angew. Chem.* **132**, 2082–2086 (2020).

(35) Gu, J. et al. Robust Superhydrophobic/Superoleophilic Wrinkled Microspherical MOF@rGO Composites for Efficient Oil–Water Separation. *Angew. Chem. Int. Ed.* **58**, 5297–5301 (2019).

(36) Jayaramulu, K. et al. Biomimetic Superhydrophobic/Superoleophilic Highly Fluorinated Graphene Oxide and ZIF-8 Composites for Oil-Water Separation. *Angew. Chem., Int. Ed.* **55**, 1178−1182 (2016).

(37) Duan, B. et al. Hydrophobic Modification on Surface of Chitin Sponges for Highly Effective Separation of Oil. *ACS Appl. Mater. Interfaces* **6**, 19933–19942 (2014).

(38) Li, L. et al. Ultrastable Triazine-Based Covalent Organic Framework with an Interlayer Hydrogen Bonding for Supercapacitor Applications. *ACS Appl. Mater. Interfaces* **11**, 26355−26363 (2019).

(39) Chandra, S. et al. Molecular Level Control of the Capacitance of Two-Dimensional Covalent Organic Frameworks: Role of Hydrogen Bonding in Energy Storage Materials. *Chem. Mater.* **29**, 2074–2080 (2017).

(40) Xu, F. et al. Radical Covalent Organic Frameworks: A General Strategy to Immobilize Open-Accessible Polyradicals for High-Performance Capacitive Energy Storage. *Angew. Chem., Int. Ed.* **54**, 6814–6818 (2015).

(41) Khayum, M. A. et al. Convergent Covalent Organic Framework Thin Sheets as Flexible Supercapacitor Electrodes. *ACS Appl. Mater. Interfaces* **10**, 28139−28146 (2018).

(42) Khattak, A. M. et al. A Redox-Active 2D Covalent Organic Framework with Pyridine Moieties Capable of Faradaic Energy Storage. *J. Mater. Chem. A* **4**, 16312−16317 (2016).

(43) Li, T. et al. A 2D covalent organic framework involving strong intramolecular hydrogen bonds for advanced supercapacitors. *Polym. Chem.* **11**, 47–52 (2020).
(44) Sun, B. et al. Interfacial synthesis of ordered and stable covalent organic frameworks on amino-functionalized carbon nanotubes with enhanced electrochemical performance. *Chem. Commun.* **53**, 6303−6306 (2017).
(45) Sun, J. et al. A Molecular Pillar Approach To Grow Vertical Covalent Organic Framework Nanosheets on Graphene: Hybrid Materials for Energy Storage. *Angew. Chem. Int. Ed.* **57**, 1034–1038 (2018).

Acknowledgements

This work was financially supported by the China Scholarship Council (CSC) and the Deutsche Forschungsgemeinschaft (DFG, German Research Foundation) under Germany's Excellence Strategy – EXC 2008/1 (UniSysCat) − 390540038. We thank Mr. Jun Wang, Mrs. Christina Eichenauer, Mrs. Maria Unterweger and Mrs. Jana Lutzki for their assistance.

Author contributions

C.L. conceived and designed the experiments. J.Y. performed the synthesis of Tp. C.L. performed all performance measurements. J. Y., C.L. and P.P. contributed to the discussion of the synthesis of COF. C.L. and S.L. contributed to the discussion of the electrochemical data. M.Y. conducted the SEM analysis. J. S. analysed the N_2 adsorption data. C.L. and A.T. wrote the manuscript. A.T. supervised the project. All authors discussed the results and commented on the manuscript.

Competing interests

The authors declare no competing interests.

Additional information

Supplementary information is available for this paper.

Correspondence and requests for materials should be addressed to A.T.

Supplementary Information

Ultralight covalent organic framework/graphene aerogels with hierarchical porosity

Changxia Li, Jin Yang, Pradip Pachfule, Shuang Li, Mengyang Ye, Johannes Schmidt and Arne Thomas*

Department of Chemistry, Division of Functional Materials, Technische Universität Berlin, Hardenbergstraße 40, 10623 Berlin, Germany

*e-mail: arne.thomas@tu-berlin.de

Materials.

All chemicals were purchased from commercial sources and used without further treatment. p-Toluenesulfonic acid monohydrate (Sigma-Aldrich, ≥ 98.5%), Diaminoanthraquinone (TCI, > 97.0%), Dimethyl sulfoxide (DMSO) (Carl Roth, ≥ 99.5%), Phenoxin (Sigma-Aldrich, > 99.5%), Methanol (Carl Roth, ≥ 99%), Tetrahydrofuran (Acros Organics, 99+%), Chloroform (Carl Roth, ≥ 99.5%), Silicone oil (Carl Roth), Hexane (Fisher, > 99%), Cyclohexane (Carl Roth, ≥ 99.5%), Toluene (Carl Roth, ≥ 99.5%), Ethyl acetate (Sigma-Aldrich, 99.8%), Acetone (Carl Roth, ≥ 99.5%), N,N-Dimethylformamide (DMF) (Carl Roth, ≥ 99.9%), Ethylene glycol (Sigma-Aldrich, 99.8%), Dioxane (Carl Roth, ≥ 99.8%), Ethanol (Carl Roth, ≥ 99.8%), N,N-Dimethylacetamide (DMA) (Carl Roth, ≥ 99%), Oil Red O (Alfa Aesar).

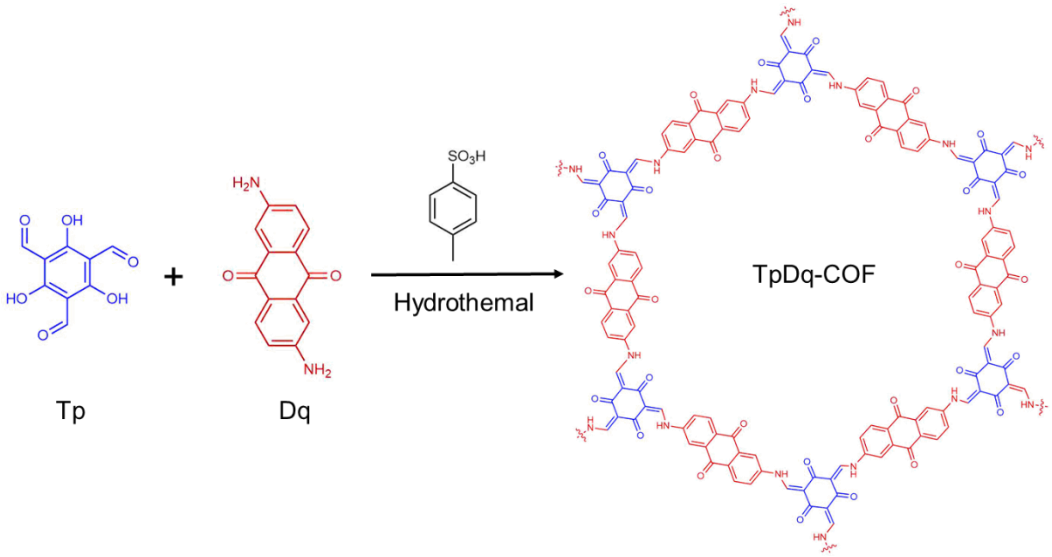

Supplementary Figure 1. Schematic representation of the synthesis of the TpDq-COF.

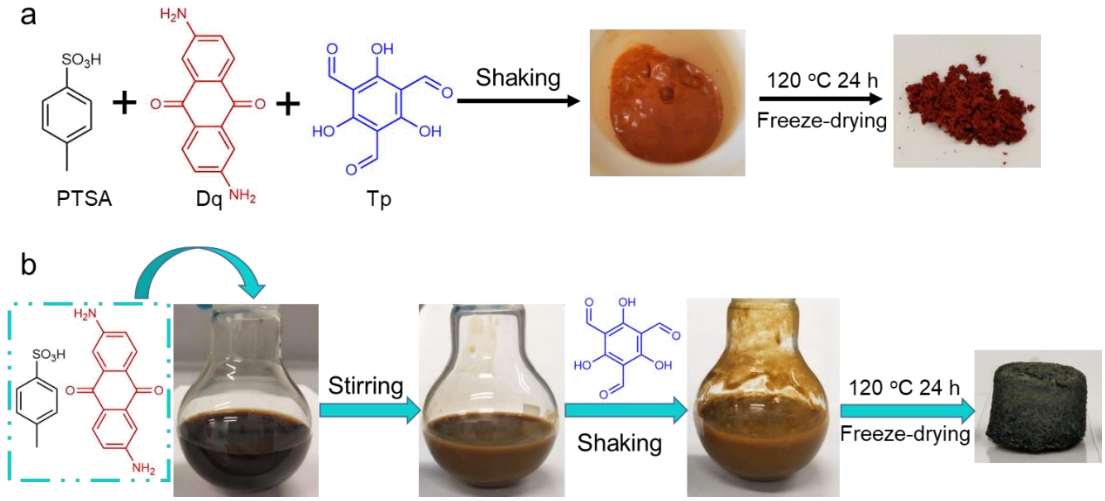

Supplementary Figure 2. Synthesis of (a) TpDq-COF and (b) COF/rGO aerogel *via* the hydrothermal method.

Supplementary Figure 3. The photograph of 5.0 mg mL^{-1} GO solution.

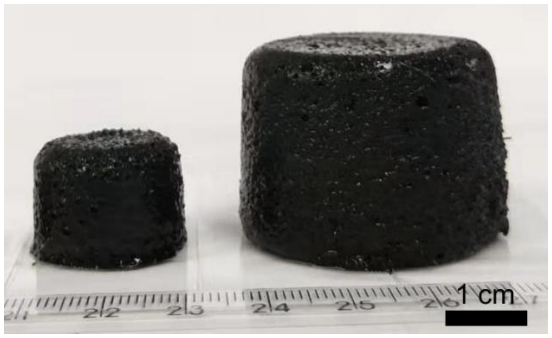

Supplementary Figure 4. A photograph of COF/rGO hydrogels prepared by using 20 ml (left) and 120 ml (right) autoclave, respectively.

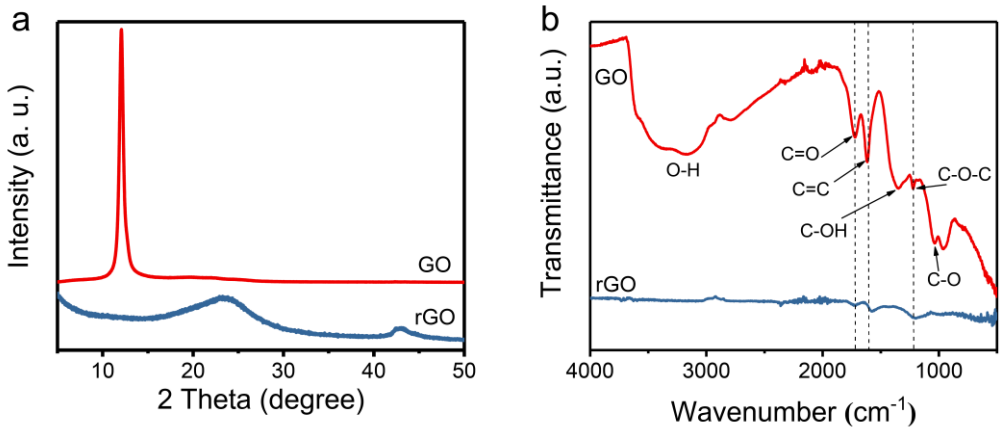

Supplementary Figure 5. (a) XRD patterns and (b) IR spectra of GO and rGO.

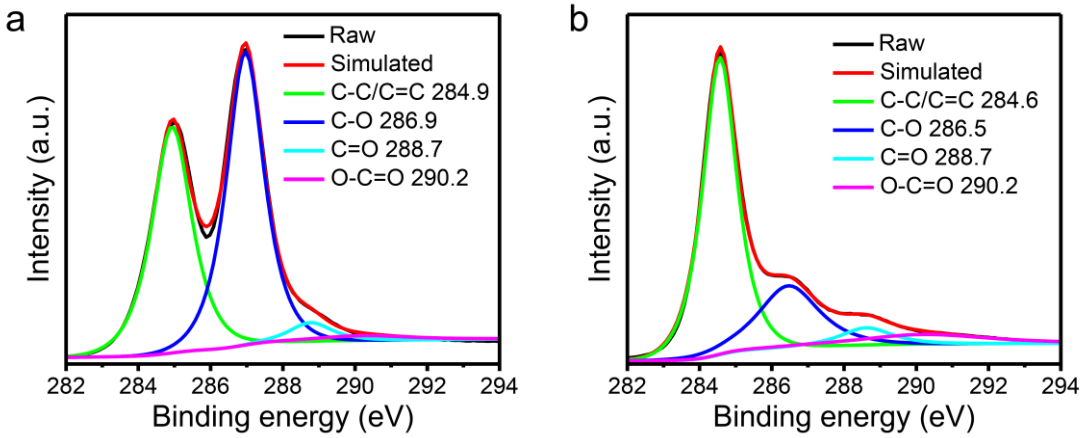

Supplementary Figure 6. XPS spectra for the C 1s peak of (a) GO and (b) rGO.

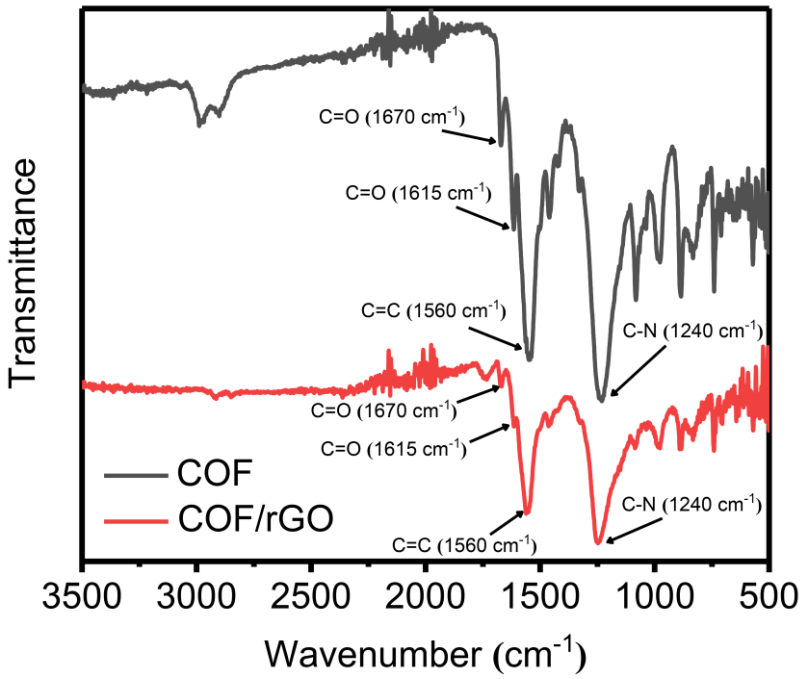

Supplementary Figure 7. IR spectra of COF and COF/rGO.

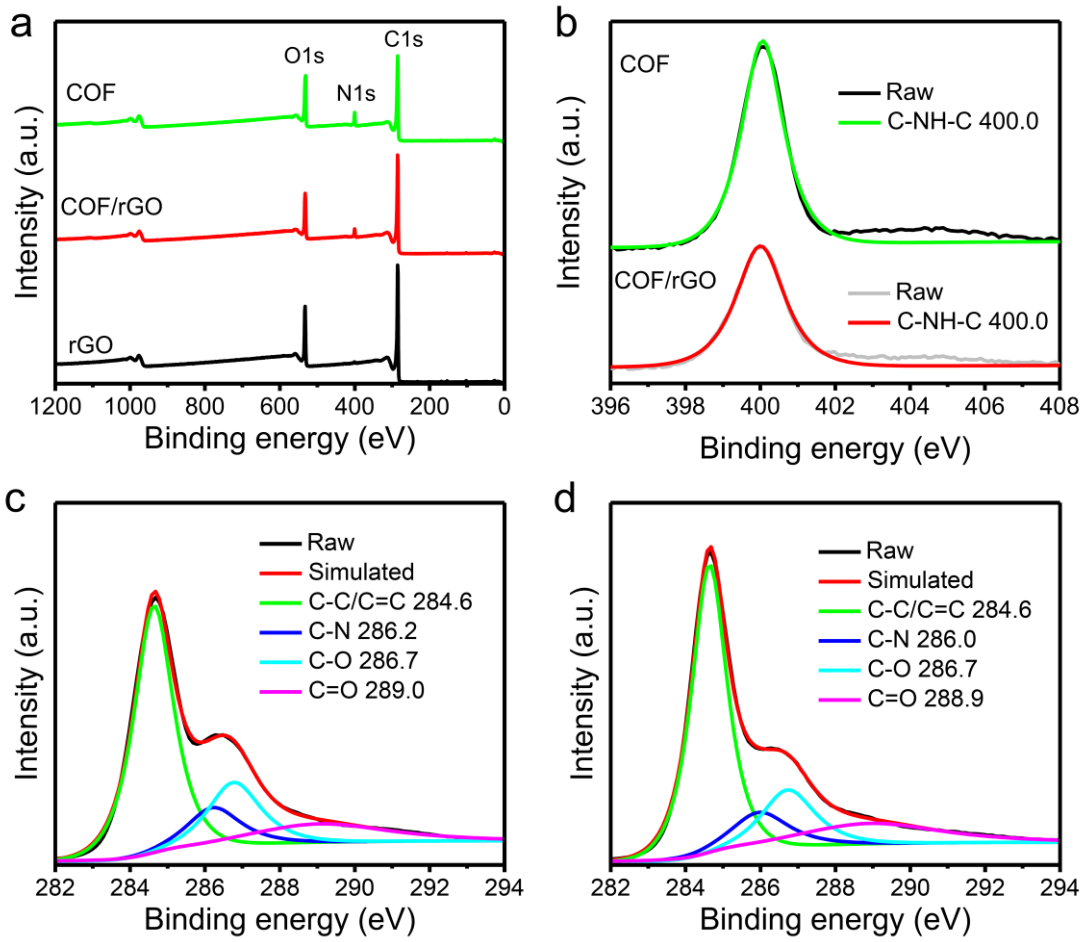

Supplementary Figure 8. (a) XPS survey spectra of COF, COF/rGO and rGO. (b) XPS spectra for the N 1s peak of COF and COF/rGO. XPS spectra for the C 1s peak of (c) COF and (d) COF/rGO.

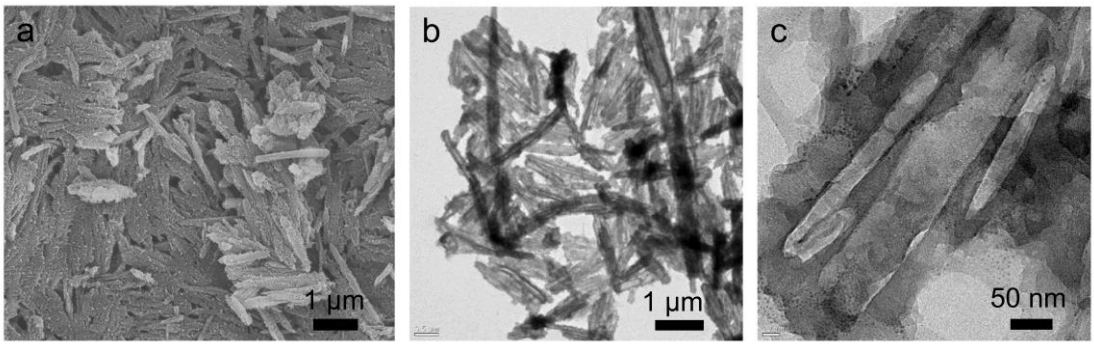

Supplementary Figure 9. (a) SEM image, and (b,c) TEM images of TpDq-COF.

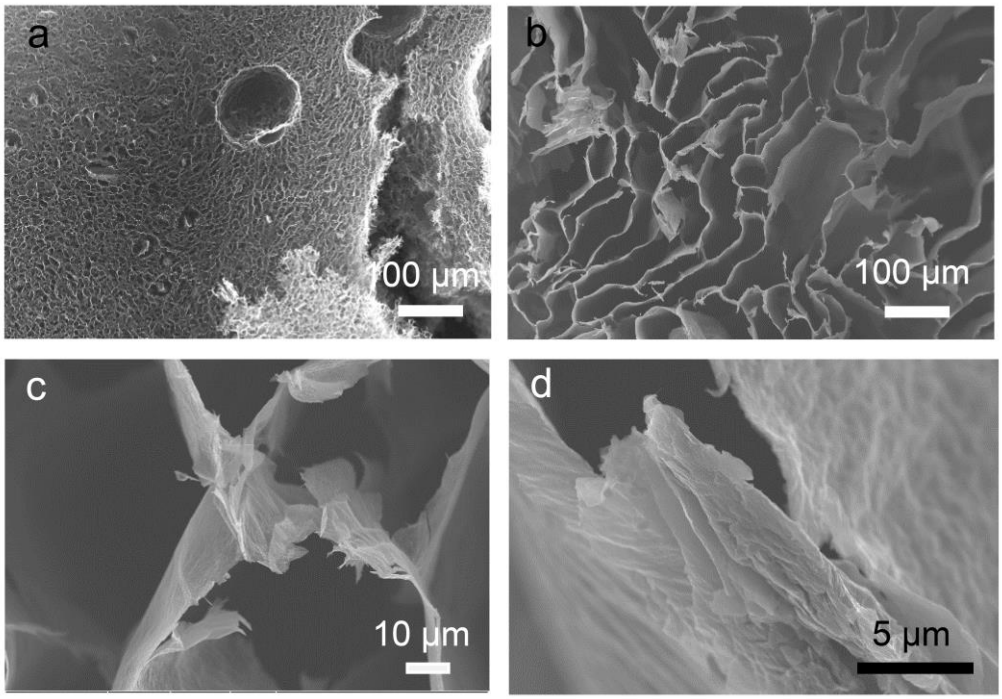

Supplementary Figure 10. SEM images of (a) COF/rGO aerogel, and (b-d) rGO aerogel.

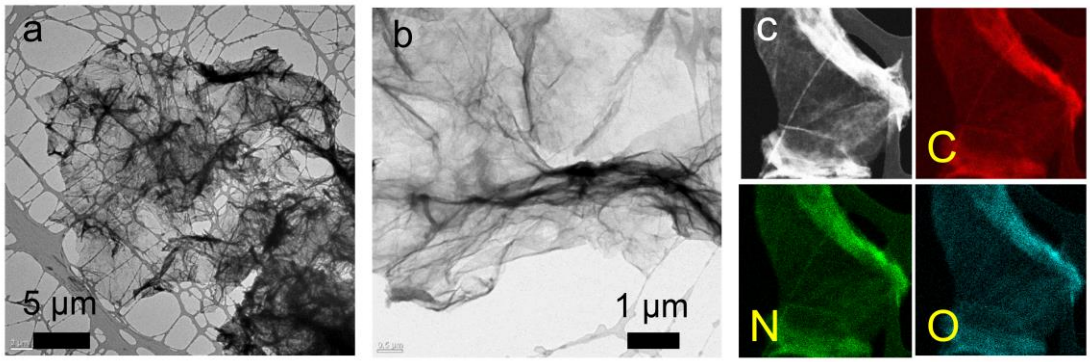

Supplementary Figure 11. (a,b) TEM image of COF/rGO. (c) STEM-EDS elemental mapping images of COF/rGO.

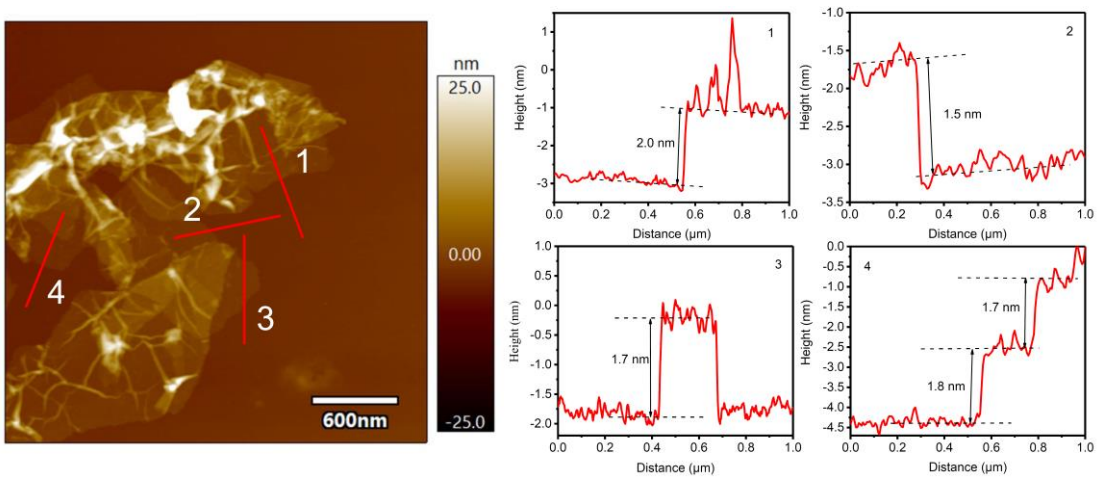

Supplementary Figure 12. AFM image and the corresponding height profiles for rGO.

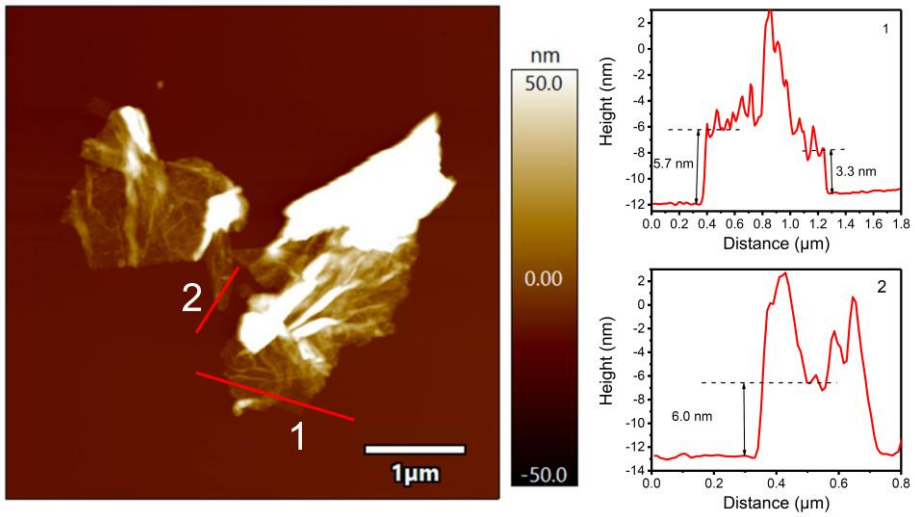

Supplementary Figure 13. AFM image and the corresponding height profiles for COF/rGO.

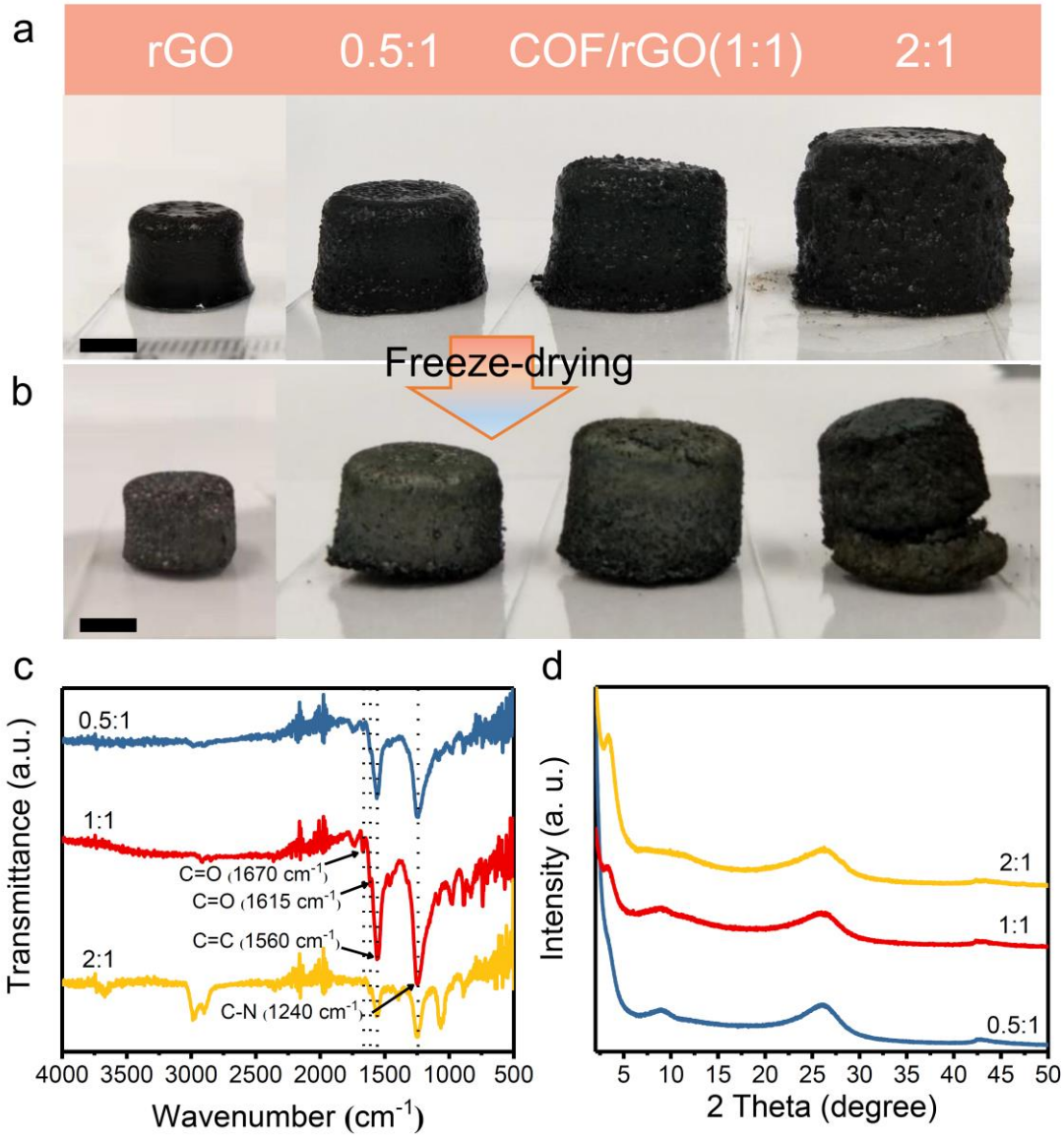

Supplementary Figure 14. 3D hydrogels and aerogels prepared from different ratio of COF monomers and GO. Photographs of (a) rGO hydrogel, COF/rGO hydrogels prepared with different amounts of COF, and (b) the corresponding aerogels after freeze-drying. The scale bar: 0.5 cm. (c) IR spectra and (d) XRD patterns of COF/rGO hybrids prepared with different amounts of COF.

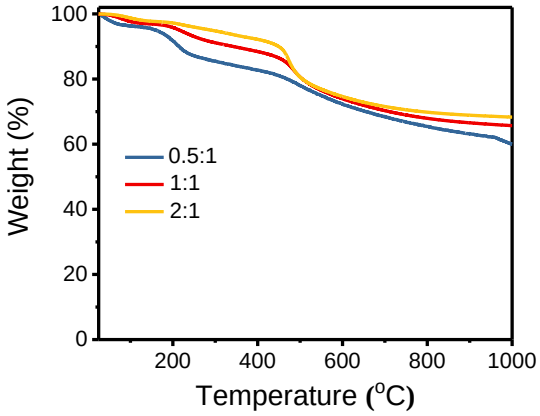

Supplementary Figure 15. TGA curves of COF/rGO hybrids prepared with different amounts of COF.

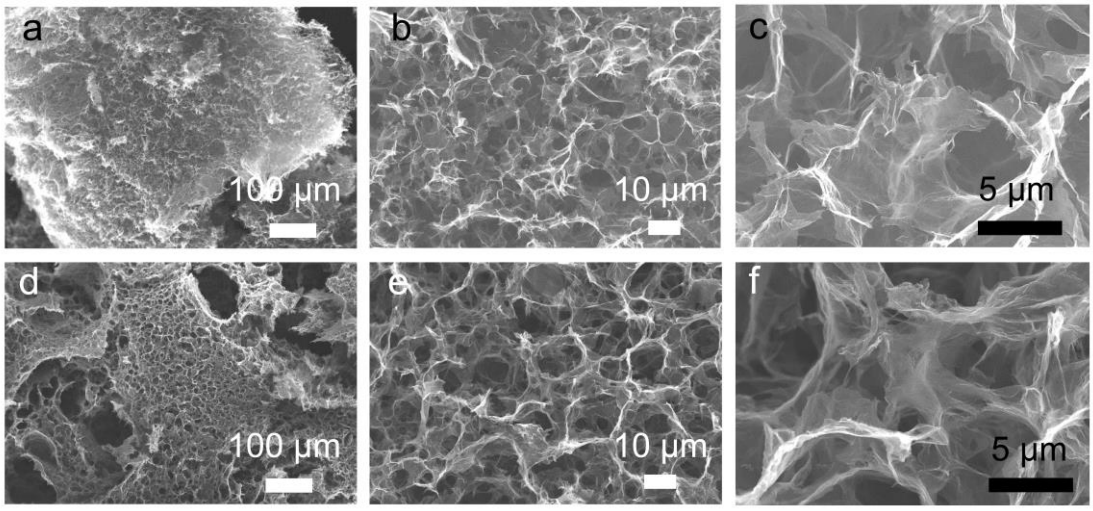

Supplementary Figure 16. SEM images of COF/rGO aerogels prepared with different amounts of COF: (a–c) 0.5:1, and (d–f) 2:1.

The SEM images exhibit the morphology change with the introduction of different ratios of COF. As shown in Supplementary Fig. 10b–d, the original rGO aerogel shows severe self-stacking with the pore size of several hundred micrometers with very thick pore walls. The self-stacking phenomenon of graphene sheets has been alleviated with the monomers: GO weight ratio of 0.5:1 (Supplementary Fig. 16a–c). For the introduction of more COF, the COF are uniformly assembled into interlinked

3D network. The COF are able to effectively prevent GO from self-stacking during the hydrothermal process. However, too much COF will break the cross-linking of GO sheets, leading to incomplete aerogel after freeze-drying (Supplementary Fig. 14b).

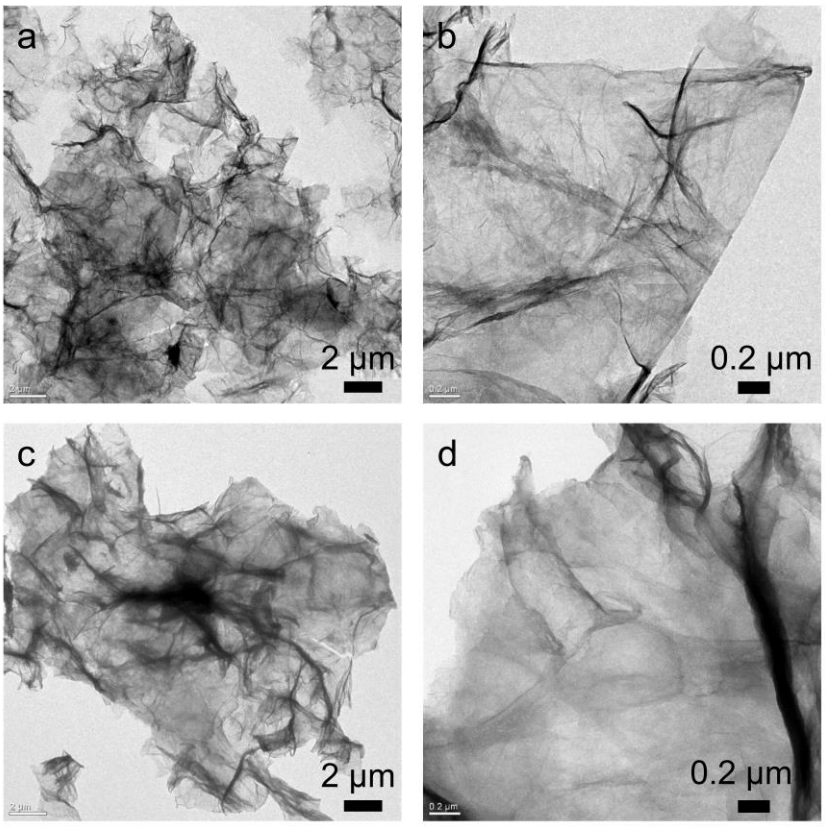

Supplementary Figure 17. TEM images of COF/rGO hybrids prepared with different amounts of COF: (a-c) 0.5:1, and (d-f) 2:1.

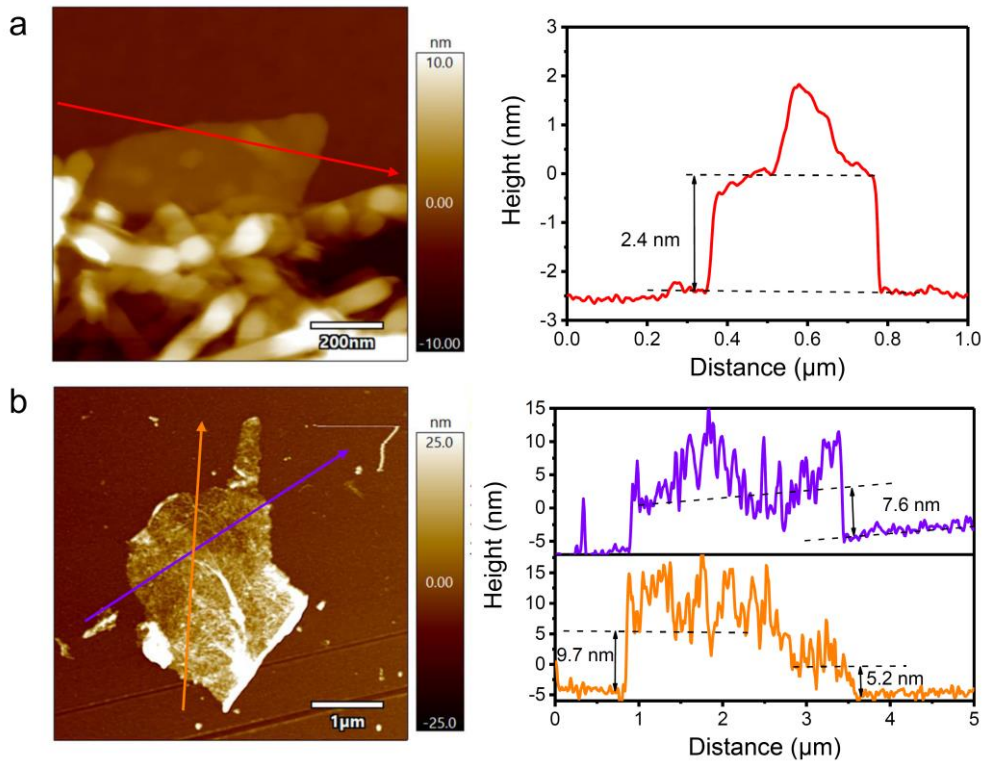

Supplementary Figure 18. AFM images and the corresponding height profiles for COF/rGO of (a) 0.5:1 and (b) 2:1.

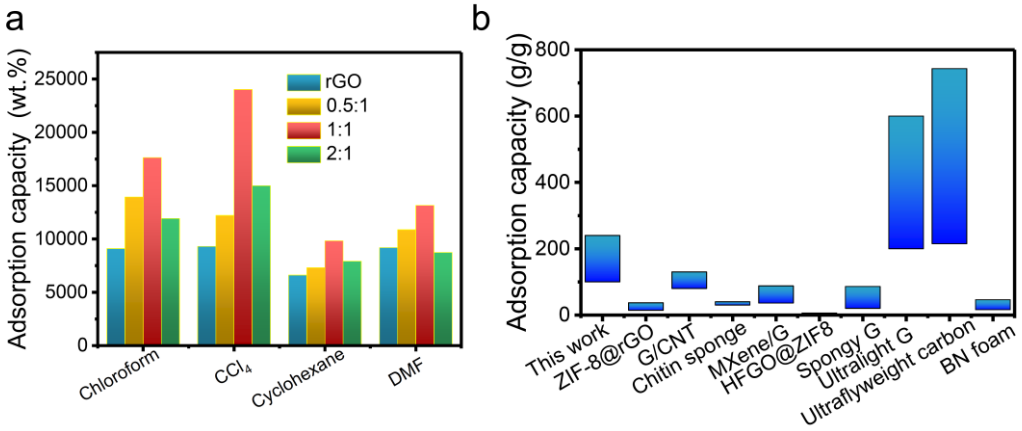

Supplementary Figure 19. (a) Adsorption efficiency of rGO and COF/rGO hybrids prepared with different amounts of COF. (b) The comparison of adsorption capacities of different graphene-based or carbon-based materials.

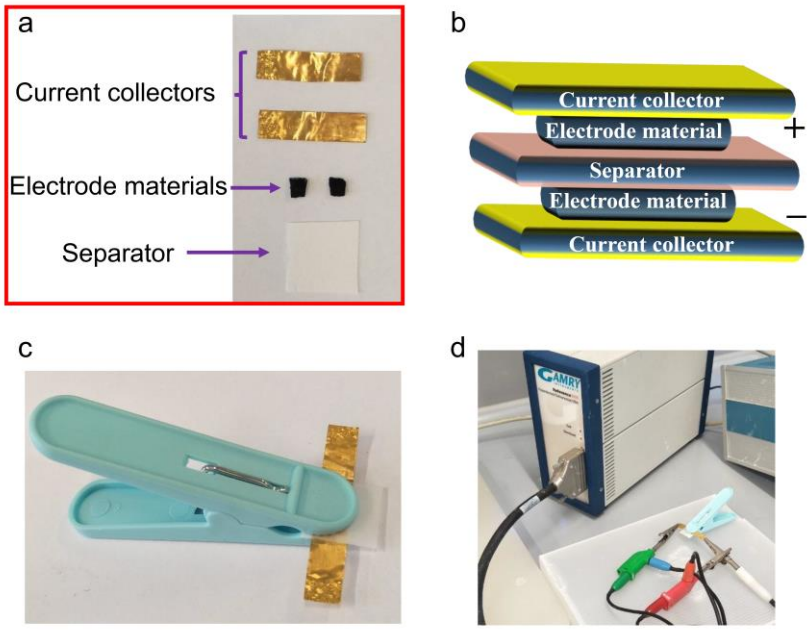

Supplementary Figure 20. A two-electrode symmetrical supercapacitor assembly. A filter paper separator soaked with 0.5 M H_2SO_4 aqueous electrolyte was used as separator and Au plates were used as current collectors. The whole device is fixed with a clip and wrapped with cling film to prevent the electrolyte from volatilizing.

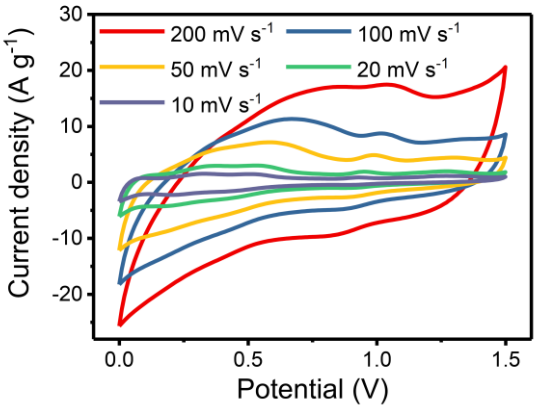

Supplementary Figure 21. CV curves of COF/rGO.

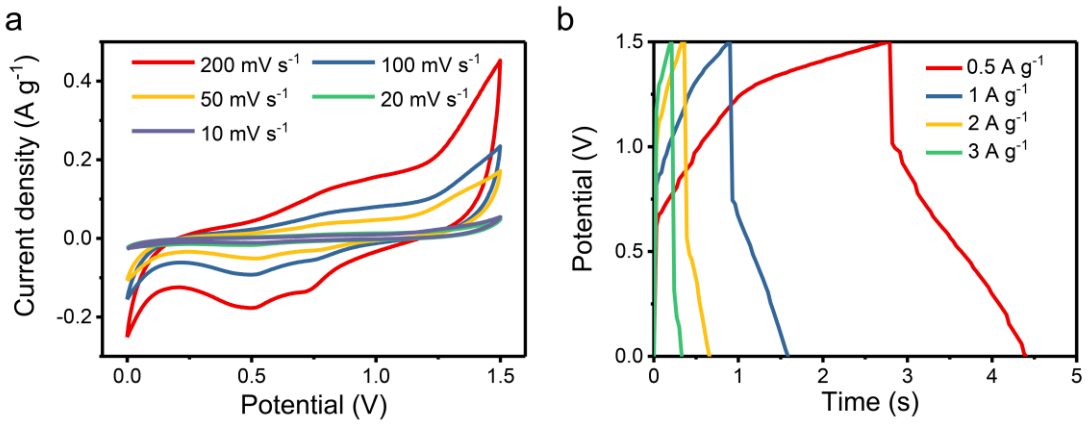

Supplementary Figure 22. (a) CV curves of COF. (b) The galvanostatic charge-discharge curves of COF.

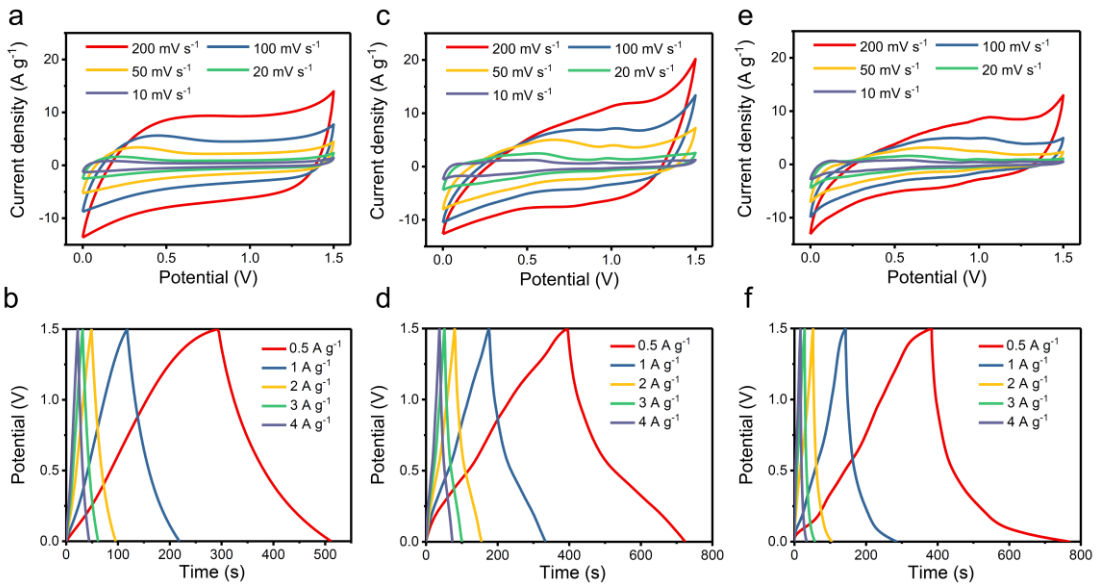

Supplementary Figure 23. CV curves of (a) rGO, (c) 0.5:1 and (e) 2:1. The galvanostatic charge-discharge curves of (b) rGO, (d) 0.5:1 and (f) 2:1.

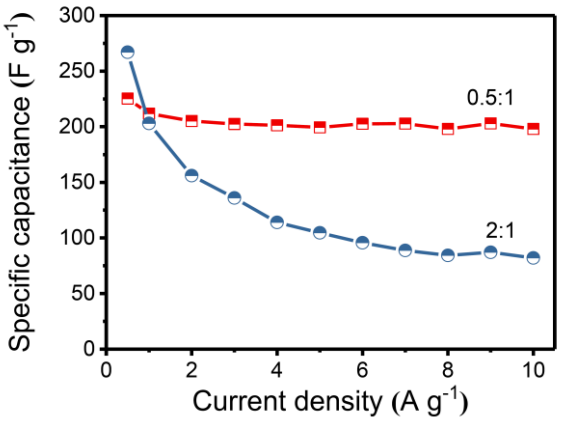

Supplementary Figure 24. The specific capacitances calculated from the discharge curves under different current density.

Supplementary Table 1. The density and element analysis results for different materials.

Samples	Density (mg cm^{-3})	C%	H%	N%
rGO	13±1.8	67.88	0.95	0.07*
0.5:1	7.5±0.4	69.82	2.05	2.42
1:1	7.0±0.5	69.11	2.06	4.52
2:1	9.0±0.8	67.32	2.3	4.9
COF	-	64.12	3.2	7.72

* Lower than the detection limit of the instrument. N% for rGO should be 0%

Based on that the N% for rGO is 0%, the COF loading weight percentage in COF/rGO hybrids can be figured out.

For 0.5:1, COF% = N% (0.5:1)/ N% (COF) = 2.42/7.72 × 100% = 31.3%.

For 1:1, COF% = N% (1:1)/ N% (COF) = 4.52/7.72 × 100% = 58.5%.

For 2:1, COF% = N% (2:1)/ N% (COF) = 4.9/7.72 × 100% = 64.0%.

Supplementary Table 2. Adsorption capacities and density of typical adsorbents.

Materials	Density (mg cm^{-3})	Adsorption substances	Capacity (g/g)	Reference
COF/rGO	7.0±0.5	Hexane, Cyclohexane, Methanol, Toluene, DMSO, Silicone oil, Chloroform, Phenixin, Ethyl acetate, Acetone, DMF, Ethylene glycol, Dioxane, Ethanol, DMA, THF	98–240	This work
ZIF-8@rGO @Sponge	-	n-Heptane, ethyl acetate, dibromoethane, butanone, acetone, toluene, tetrachloromethane, chloroform, silicone oil, bump oil, bean oil	14–37	*Angew. Chem. Int. Ed*. **58**, 5297–5301 (2019)
Graphene–CNT hybrid foam	6.92	Compressor oil, sesame oil, chloroform, dichlorobenzene, toluene, DMF	80–130	*Chem. Commun.* **48**, 10660–10662 (2012).
Chitin sponges	20.1	Hexane, Gasoline oil, Cyclohexane, Corn oil, Toluene, Silicone oil, Pump oil, Engine oil, Chloroform, Phenixin	30–40	*ACS Appl. Mater. Interfaces* **6**, 19933–19942 (2014)
MXene/G	27	Hexane, Octane, Decane, Cyclohexane, Ethyl acetate, Acetone. DMF, Ethylene glycol, DMSO, Pump oil, Dioxane, Toluene, Phenoxin, THF, Dodecane	36–88	*Angew. Chem. Int. Ed*. **58**, 5297–5301 (2019)
BN	30.4	Formamide, Hexane, DMF, Benzene, 1-Butanol, Ethanol, Acetone, Salad oil, Dioxane, Oleic acid, Pumping oil, Dibutylphthalate, Silicone oil, Chloroform	16–46	*ACS Nano* **11**, 558−568 (2017)
FGO@MOG	-	toluene, hexane, heptane, decane, octadecane, petroleum ether, crude oil, veg oil, carbon tetrachloride	3–5	*Adv. Mater.* **29**, 1605307 (2017)
Spongy graphene	12	Methanol, Ethanol, Acetone, THF, DMSO, Toluene, Soybean oil, Caster oil, Kerosene, Pump oil, Dodecane, Decane, Octane, Heptane, Hexane, Nitrobenzene, Chloroform, 1,2-dichlorobenzene,	20–86	*Adv. Funct. Mater.* **22**, 4421–4425 (2012)

		Ethylbenzene		
Ultralight graphene framework	2.1±0.3	Ethanol, Acetone, Phenoxin, Cyclohexane, Chlorobenzene, Olive oil, Tetrahydrofuran (THF), Methanol, Toluene, Dimethyl sulfoxide (DMSO), Chloroform, Nitrobenzene, Gasoline	200–600	*Angew. Chem. Int. Ed*. **51**, 11371–11375 (2012)
Ultra-flyweight carbon aerogel	1.4	Hexane, Ethanol, Crude oil, Toluene, Motor oil, Veg oil, Dioxane, Ionic liquid (1-butyl-3-methylimidazolium tetrafluoroborate), Chloroform, Phenixin	215–743	*Adv. Mater.* **25**, 2554–2560 (2013).
HFGO@ZIF-8	-	Vegetable oil, Decaoctane, silicone oil, coconut oil, petroleum ether, chloroform	1.5–6	*Angew. Chem. Int. Ed*. **55**, 1178–1182 (2016).
Fe_2O_3/C foam	8.9	crude oil, bean oil, lubricating oil, hexane, gasoline, diesel oil, octane, decane, dodecane	60–102.6	*ACS Nano* **7**, 6875–6883 (2013).

Supplementary Table 3. Comparison of specific capacitances for different COFs based materials.

Materials	Potential window (V)	Capacitance (F/g)	Retention	Ref.
COF/rGO	**0–1.5**	**269 at 0.5 A g^{-1}**	**96% after 5000 cycles**	**Present work**
PDC-MA-COF	0–1.5	94 F g^{-1} at 1.0 A g^{-1}	88%% after 20000 cycles	*ACS Appl. Mater. Interfaces* **11**, 26355–26363 (2019)
TpPa-$(OH)_2$	0–0.7	214 F g^{-1} at 0.2 A g^{-1}	88% after 10000 cycles	*Chem. Mater.* **29**, 2074–2080 (2017)
DAAQ-TFP COF*	-0.3–0.3	48±10 at 10 mV s^{-1}	82% after 5000 cycles	*J. Am. Chem. Soc.* **135**, 16821–16824 (2013)
$[TEMPO]_{100\%}$-NiP-COF $[TEMPO]_{50\%}$-NiP-COF	0–0.8	(i) 167 at 0.1 A g^{-1} (ii) 124 0.1 A g^{-1}	(i) 81% after 2000 cycles (ii) 70% after 2000 cycles	*Angew. Chem. Int. Ed.* **54**, 6814–6818 (2015)
Dq_1Da_1Tp COF DqTp COF	0–1	111 F g^{-1} at 1.56 mA cm^{-2} 154 F g^{-1} at 1.56 mA cm^{-2}	90% after 2500 cycles; 80% after 2500 cycles	*ACS Appl. Mater. Interfaces* **10**, 28139–28146 (2018)
COF/NH_2-rGO*	0–0.5	533 at 0.2 A g^{-1}	79% after 1000 cycles	*RSC Adv.* **5**, 27290–27294 (2015)
TaPa-Py COF	0–0.8	102 at 0.5 A g^{-1}	92% after 6000 cycles	*J. Mater. Chem. A* **4**, 16312−16317 (2016)
TPT-DAHQ COF*	-1–0.5	256 at 0.5 A g^{-1}	98.8% after 1850 cycles	*Chem. Asian J.* **14**, 1429–1435 (2019)
TpOMe-DAQ*	-0.5–0.5	169 at 0.35 A g^{-1}	increment after 30000 cycles	*J. Am. Chem. Soc.* **140**, 10941–10945 (2018)
v-CNS-RGO	-0.5–0.5 A/g	ca. 165 at 0.5 A g^{-1}	ca. 100% after 3000 cycles	*Angew. Chem. Int. Ed.* **57**, 1034–1038 (2018)
Ni3(HITP)2*	0–1	111 at 0.05 A g^{-1}	90% after 10000 cycles	*Nat. Mater.* **16**, 220–224 (2017)

TPA–TPA-COF-1*	0.2–0.7	51.3 at 0.2 A g^{-1}	-	*J. Mater. Chem. A* **6**, 19532–19541 (2018)
TFP–NDA–COF*	0–1	379 F g^{-1} at 2 mV s^{-1}	75% after 8000 cycles	*Microporous Mesoporous Mater.* **266**, 109–116 (2018)
$COF_{BTA-DPPD}$-rGO*	0–0.5	239.1 F g^{-1} at 0.5 A g^{-1}	70% after 1500 cycles	*Microporous Mesoporous Mater.* **287**, 65–70 (2019)
AC//PG-BBT	0–1.5	220 F g^{-1} at 1 A g^{-1}	-	*Polym. Chem.* **11**, 47–52 (2020)
Car-TPT COF*	0–0.6	17.4 F g^{-1} at 0.2 A g^{-1}	-	*ACS Appl. Mater. Interfaces* **11**, 9343–9354 (2019)
NH_2-f-MWCNT @$COF_{TTA–DHTA}$	0–0.8	127.5 F g^{-1} at 0.4 A g^{-1}	96% after 1000 cycles	*Chem. Commun.* **53**, 6303−6306 (2017)

*The capacitances were measured in three-electrode systems.